DOI: 10.1021/ma902105v

Macromolecules
ARTICLE

An *in Situ* X-ray Structural Study of Olefin Block and Random Copolymers under Uniaxial Deformation

Feng Zuo, Christian Burger, Xuming Chen, Yimin Mao, and Benjamin S. Hsiao*

Department of Chemistry, Stony Brook University, Stony Brook, New York 11794

Hongyu Chen, Gary R. Marchand, Shih-Yaw Lai, and Debbie Chiu

The Dow Chemical Company, Freeport, Texas 77541

Received September 22, 2009; Revised Manuscript Received December 26, 2009

ABSTRACT: The structure, morphology, and orientation development during deformation of an olefin block copolymer (OBC) and an olefin random copolymer (ORC), based on ethylene−octene composition and with similar overall density, were investigated by *in situ* synchrotron X-ray scattering and diffraction techniques at room temperature and 60 °C. It was found that the original OBC contained only orthorhombic crystals, while the original ORC contained mixed orthorhombic and hexagonal crystals. Under deformation at room temperature, monoclinic crystals were induced in both polymers due to the transformation of orthorhombic crystals under elongation. Under deformation at 60 °C, as monoclinic crystals are thermally unstable, the orthorhombic form became dominant. Upon stretching, the crystal structure in ORC became aligned with a higher degree of orientation along the drawing direction than that of OBC. This different behavior could be attributed to the low chain shuttling agent level of studied OBC, resulting in relatively broader molecular weight distribution and very few hard and soft blocks in one polymer chain, and high octene comonomer content in soft blocks and thus low-density noncrystallizable blocks. Both factors lead to a less effective network structure under deformation than that of ORC with the same density.

Introduction

In the preparation of olefin random copolymers (ORCs), such as random ethylene copolymers, the content of comonomer (e.g., propene, butene, hexene, or octene, etc.) can directly affect the properties of the final products. Usually, the higher the comonomer content, the better the elastomeric property. However, since the melting temperature also decreases with the increase in comonomer content, a copolymer with high comonomer content has limited value for applications at high temperatures. Recently, a novel class of olefin block copolymers (OBCs) was produced by scientists at The Dow Chemical Company using innovative chain shuttling technology.[1−5] This technology employs two catalysts with different monomer selectivity and one chain shuttling agent which can reversibly transfer the growing chains between two catalysts. The resulting OBC microstructure comprises alternating hard blocks having high or medium density and soft blocks having low density. As the hard block contains low comonomer content, it possesses a high melting point; because the soft block contains high comonomer content, it behaves as an amorphous chain with a low glass transition temperature. Thus, a major advantage of an OBC is that it can exhibit excellent elastomeric properties and have high thermal stability (up to 125 °C) due to the high melting point of the hard blocks (the typical melting point of ORC of the same composition is tens of degrees lower). In addition, there are more controllable parameters during the production of OBC than in ORC, such as block length, block distribution, and comonomer contents in the hard and soft blocks, making the production of OBCs with varying structures possible. It has been shown that OBCs exhibit better mechanical recovery, abrasion resistance, and compression set than random ethylene copolymers, indicating that OBCs are promising for many applications.[6]

The structure and mechanical properties of ORCs, such as ethylene−octene random copolymers, have been studied extensively before.[7−14] In this study, our objective is to understand the relationships among chain architecture, crystal structure, morphology, and properties in OBCs and their difference with ORCs. The results will benefit the design of OBC and thus produce more desirable products for different applications. The chosen copolymer system was ethylene−octene block and random copolymers, which were subjected to uniaxial deformation at room temperature and high temperature and studied by *in situ* synchrotron X-ray scattering and diffraction techniques. Specifically, time-resolved two dimension (2D) wide-angle X-ray diffraction (WAXD) and small-angle X-ray scattering (SAXS) measurements were carried out during uniaxial stretching deformation. The results revealed a clear difference in structure and morphology changes between the two samples under deformation and allowed us to propose probable reasons due to the difference in chain architecture.

Experimental Section

Materials and Preparation. In this study, two polymer samples were chosen, all provided by The Dow Chemical Company. One was an OBC with ethylene and octene as comonomers; the other one was ethylene−octene random copolymer. The information about the overall density, weight-averaged molecular weight, and the molecular weight distribution is listed in Table 1. Both OBC and ORC had the same overall density. However, the OBC consisted of 21 wt % hard block (containing 0.4 mol % octene comonomer) with density of 0.932 g/cm^3 and 79 wt %

*To whom correspondence should be addressed: e-mail bhsiao@notes.cc.sunysb.edu; Tel 631-632-7793; Fax 631-632-6518.

 Published on Web 01/25/2010

Table 1. Sample Information of OBC and ORC

	overall density (g/cm^3)	soft block wt %	soft block density (g/cm^3)	hard block density (g/cm^3)	M_w (kg/mol)	M_w/M_n
OBC	0.875	79	0.857	0.932	124	3.05
ORC	0.875		ethylene−octene random copolymer		79	2.47

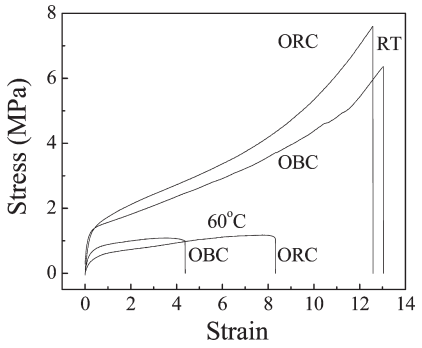

Figure 1. Engineering stress−strain curves of OBC and ORC at room temperature and 60 °C.

soft block (containing 16.7 mol % octene comonomer) with density of 0.857 g/cm^3. Thus, based on the perspective of density, only the hard blocks in the OBC could crystallize at room temperature and above, while soft blocks would remain amorphous. The density of homogeneous random copolymer (containing 11 mol % octene comonomer) was 0.875 g/cm^3, for comparison to the hard blocks in OBC. The molecular weight distribution of ORC was 2.47, while that of OBC was relatively broader, 3.05. The broader molecular weight distribution of OBC could be due to the low chain shuttling agent level. Isotropic films of ORC and OBC were obtained by melt compression of both samples at 165 °C in a dumbbell-shaped mold and then quenching to room temperature. The dumbbell-shaped sample was 35 mm long, 6 mm wide, and 1 mm thick.

Characterization Methods. *In situ* WAXD and SAXS studies were carried out at the X27C beamline in the National Synchrotron Light Source (NSLS), Brookhaven National Laboratory (BNL). The wavelength of the synchrotron radiation was 1.371 Å. A three-pinhole collimation system was used to reduce the beam size to 0.6 mm in diameter. 2D WAXD and SAXS patterns were collected by a MAR CCD X-ray detector (MAR-USA), which had a resolution of 1024 × 1024 pixels (pixel size = 158.44 μm). The typical image acquisition time was 20 s for each data frame. The sample-to-detector distance was around 1900 mm for SAXS (calibrated by a silver behenate (AgBe) standard), and was around 110 mm for WAXD (calibrated by an aluminum oxide (Al_2O_3) standard). All X-ray images were corrected for background scattering, air scattering, and beam fluctuations.

Uniaxial tensile deformation was performed with a modified Instron 4442 tensile apparatus, which could stretch the sample symmetrically. The symmetric stretching allowed the focused X-ray beam to illuminate the same sample position during deformation. The length of the starting sample between the Instron clamps was 15 mm. A constant deformation rate, 4.5 mm/min (30%/min), was applied to the specimen throughout the deformation study. The deformation experiments were carried out at room temperature and 60 °C, respectively. The stress and strain mentioned through the article are all engineering stress and engineering strain measured directly between the clamps, and yielding stress is obtained by the crossover of the two tangents to the stress−strain curve before and after yielding. The heating chamber for this Instron apparatus was about 200 mm in length, whereby the highest attainable engineering strain was about 13.

Results and Discussion

Stress−Strain Curves. Figure 1 shows the engineering stress−strain curves of OBC and ORC during uniaxial tensile deformation at room temperature and 60 °C, respectively. The mechanical data are summarized in Table 2. Both ORC and OBC exhibited similar stress−strain curves with typical characteristics of elastomers, i.e., nondistinct yielding point compared to plastics upon deformation, steady increase of stress in the early stage, and strain hardening at the late stage of room temperature deformation. One notable difference was that ORC exhibited higher strength than OBC during deformation at room temperature, but the trend became reversed at 60 °C due to this high experimental temperature, which was close to the melting point of the random copolymer at 68 °C but far away from the melting point of OBC at 125 °C. The fracture strain of OBC was similar to ORC at room temperature, but they were quite different at 60 °C—the fracture strain of ORC was significantly higher than OBC. A potential explanation is as follows. The ORC, because of its narrower molecular weight distribution of 2.47, has a more effective amorphous network at 60 °C, as we shall see from the morphology results. On the other hand, the OBC has a broader molecular weight distribution of 3.05 due to the low chain shuttling agent level and thus a less effective network. The tensile data for OBC at 60 °C were somewhat surprising at first when one considers the melting point of the OBC was much higher. This can be explained as follows. A recent study has shown that ethylene−octene random copolymers have a comonomer content dependence of α-relaxation.[15] Low comonomer content as in hard blocks leads to large and well-organized lamellar crystals, and thus the α-relaxation process can take place at high temperature. But for high comonomer content in ORC, low crystallinity and small crystals lead to the disappearance of the α-relaxation. At 60 °C the high melting crystals can undergo α-relaxation during tensile deformation, leading to crystal slip via translation of chain segments along the crystalline axis.[16−18] Additionally, crystallization in OBC only happens within hard blocks, which are long enough without many branches to fold back and forth into lamellar crystals. After crystallization, the soft block in between two hard blocks may become a tie chain connecting the lamellar crystals. Whereas for an ORC, there is no difference in crystallizability along the whole statistical polymer chains in the ORC, and every part of the chain can possibly participate in crystallization. The schematic diagrams of OBC and ORC chains in the homogeneous melt and after crystallization are shown in Figure 2. It is seen that the high comonomer content in ORC as compared to hard blocks (colored in red) in OBC can lead to poor crystallizability and much more small crystals exceeding the number of large lamellar crystals in OBC. Thus, a single polymer chain in ORC can participate in more crystal junctions, so the number of tie chains in OBC should be less than ORC, which also means better connectivity among polymer chains and a more effective network in ORC. The difference in the octene comonomer content (0.4 mol % vs 16.7 mol %) can

Table 2. Mechanical Properties of OBC and ORC at Room Temperature and 60 °C

	fracture strain		yield stress (MPa)		fracture stress (MPa)	
	RT	60 °C	RT	60 °C	RT	60 °C
OBC	13.0	4.4	1.3	0.8	5.8	1.2
ORC	12.5	8.3	1.4	0.6	7.6	1.1

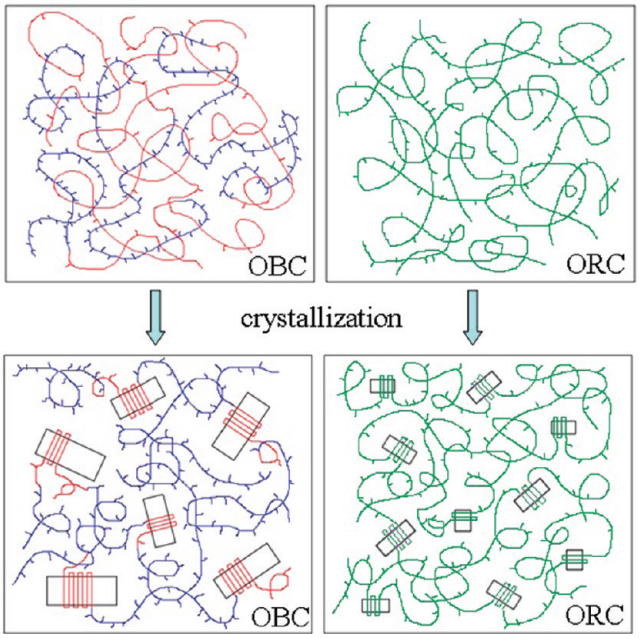

Figure 2. Schematic diagrams of OBC (left) and ORC (right) in the homogeneous melt (top) and after crystallization (bottom).

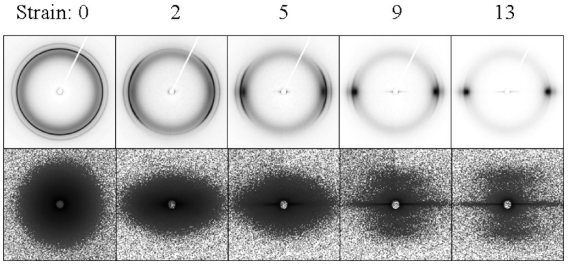

Figure 3. Selected 2D WAXD and SAXS patterns of OBC during uniaxial deformation at room temperature.

also cause the hard and soft chains (nonshuttled fragments due to low chain shuttling level) in OBC to behave more like an immiscible polymer blend after crystallization-induced phase segregation,[4] where there are no connections among these blocks.

Formation of Monoclinic Crystals under Strain. 2D SAXS and WAXD patterns of OBC at selected strains during uniaxial deformation at room temperature are shown in Figure 3. Before deformation, the WAXD pattern exhibits a broad amorphous peak at lower diffraction angle and two distinct diffraction peaks at higher angles that can be indexed as (110) and (200) reflections, respectively, from the orthorhombic form. All reflections are isotropic, indicating that the crystalline phase is unoriented in the initial sample. Upon deformation (e.g., strain = 2.0), the (110) reflection becomes four-arc-like with maximum at the off-axis position, which suggests the orientation of the crystals. Upon further deformation (e.g., strain = 5.0), the (110) reflections change from four arcs to two arcs on the equator, indicating that the crystals have a *b*-axis orientation at low strains and *c*-axis orientation at high strains. This behavior has been reported before.[19] It is also seen that at high strains the azimuthal spread of all crystal reflections becomes narrow, indicating the crystal orientation became higher. At the intermediate stage of deformation (e.g., strain = 5.0), a highly oriented but relatively diffuse point-like reflection, located between the (110) reflection and the amorphous peak, is seen on the equator.

The 3D intensity profile of OBC around the equator taken at strain = 4.0 is illustrated in Figure 4, where this new

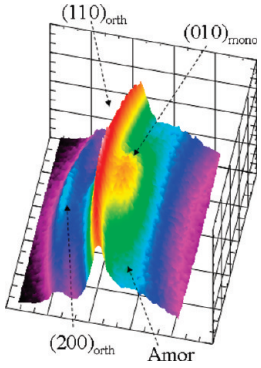

Figure 4. 3D WAXD profile around the equatorial region (the beam center is to the right) for OBC taken at strain = 4 and room temperature.

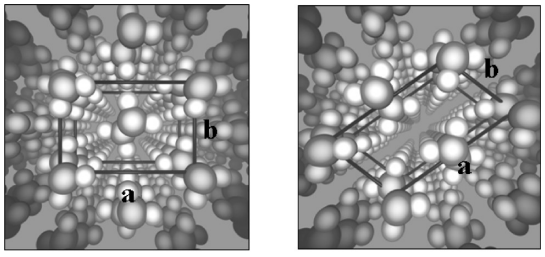

Figure 5. 3D molecular structure of orthorhombic (A) and monoclinic (B) crystals, projected along the *c*-axis.

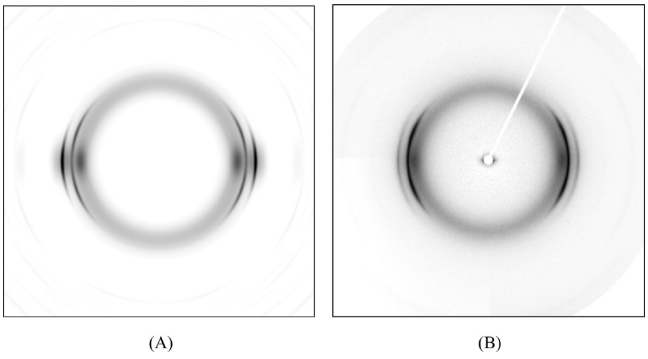

Figure 6. (A) Calculated scattering of orthorhombic and monoclinic crystals with amorphous halo. (B) Experimental scattering pattern of OBC containing amorphous, orthorhombic, and monoclinic crystals.

strain-induced reflection is distinct from the (110) reflection (colored in red) and the amorphous halo (colored in light blue and green). The new reflection is indexed as the (010) reflection from the monoclinic form of polyethylene crystals. It is generally accepted that the orthorhombic form is the most common and stable crystal form in polyethylene (PE); the hexagonal form usually occurs in defected crystals, such as random copolymer with high octene content, while the monoclinic form is usually formed under conditions of tension or compression.[20−26] The lattice structures of orthorhombic and monoclinic forms in PE are illustrated in Figure 5.

Several mechanisms of the transformation from orthorhombic to monoclinic forms have been proposed, such as slipping and twinning. Our experimental results are very consistent with the previous observations. To further verify the existence of strain-induced monoclinic phase in the chosen copolymer, we calculated a WAXD pattern for a mixture of orthorhombic and monoclinic crystals with an

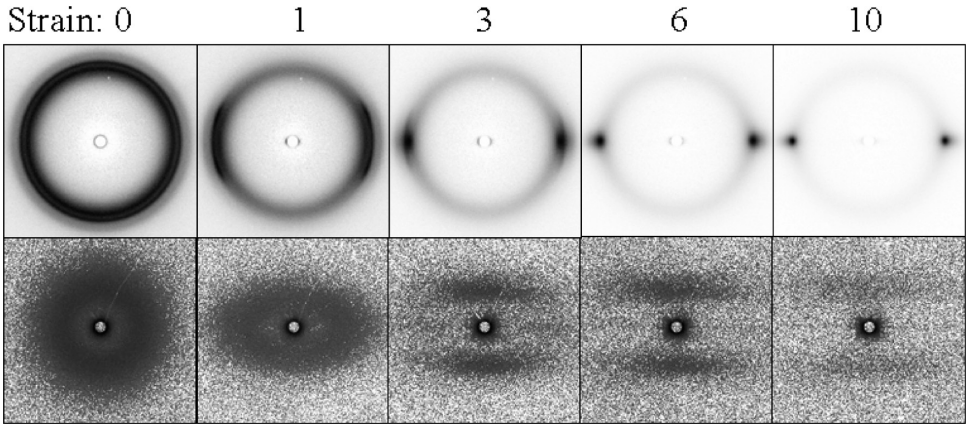

Figure 7. Selected 2D WAXD and SAXS patterns of ORC during uniaxial deformation at room temperature.

amorphous phase, and proper orientations for each crystal were carefully chosen to simulate the intensity distribution of all reflections in the measured profile. The comparison between the simulated pattern and the measured WAXD pattern is shown in Figure 6. It can be seen that the general feature of the calculated profile closely resembled that of the measured profile. The comparison also confirms the occurrence of monoclinic crystals induced by uniaxial deformation. The detailed analysis of each crystal phase under deformation is discussed later.

Morphological Changes during Deformation. In Figure 3, the 2D SAXS pattern taken from undeformed OBC exhibits a different scattering feature when compared with that of common crystalline PE. In the latter, a broad scattering peak from the layered structure of folded chain lamellar crystals is often observed, where the layered structure consists of a long period in the order of tens of nanometers. In OBC, the scattering intensity profile is found to decrease monotonically with the scattering vector. This feature can be explained by the microphase morphology in OBC as follows. The soft and hard blocks are different in chain architecture and crystallizability. Both blocks are miscible and form a homogeneous melt at high temperatures above the nominal melting point. But upon cooling the hard blocks can crystallize into lamellar structures via nucleation and growth mechanisms, and the nearby soft blocks have to be pushed away from the crystalline region into the amorphous region. Thus, the excluded soft blocks or amorphous hard segments can form tiny grain-like local domains with a slightly different electron density from the homogeneous amorphous phase. From the results, the domain-like structures in OBC are not correlated with each other, leading to a diffused scattering pattern with strong signal uptake at low angles. This domain scattering is also consistent with the low q scattering observed by others.[27−29] After the Lorentz correction, a scattering peak from the lamellar structure can be seen. With the increase in strain, some lamellar crystals could be stretched and reoriented into fibrillar form (usually hundreds of nanometers in length and several nanometers in width) along the drawing direction. The fibrillar morphology and the possible occurrence of oriented microvoids are probably responsible for the appearance of a SAXS equatorial streak at high strains (Figure 3). It is also concluded that some lamellar stacks persist with the increasing strain, since a two-bar scattering is seen on the meridian at strain > 9. Under these high strains, lamellar stacks are arranged perpendicularly (i.e., the polymer chains are parallel) to the drawing direction.

Comparison between OBC and ORC. Selected 2D WAXD and SAXS patterns of ORC during uniaxial deformation under the same deformation conditions are shown in Figure 7. In the WAXD pattern, the (110) reflection is clearly identified, but the (200) reflection is too weak to be seen. This indicates that OBC has more perfect or larger orthorhombic crystals than ORC. Comparison of integrated WAXD profiles from OBC and ORC before deformation is shown in Figure 8A. In both systems, positions of the (110) and (200) reflections are the same, consistent with the presence of orthorhombic crystal structure. ORC exhibits a broader distribution in both reflections, indicating that its crystal size was smaller than OBC. Studies carried out by Wang et al. revealed that the spherulites and lamellar structure were observed in ethylene−octene block copolymer, while only small fringed-micellar crystals were observed in ethylene−octene random copolymer.[3,29] So our structural observations are consistent with Wang's. The position of the amorphous

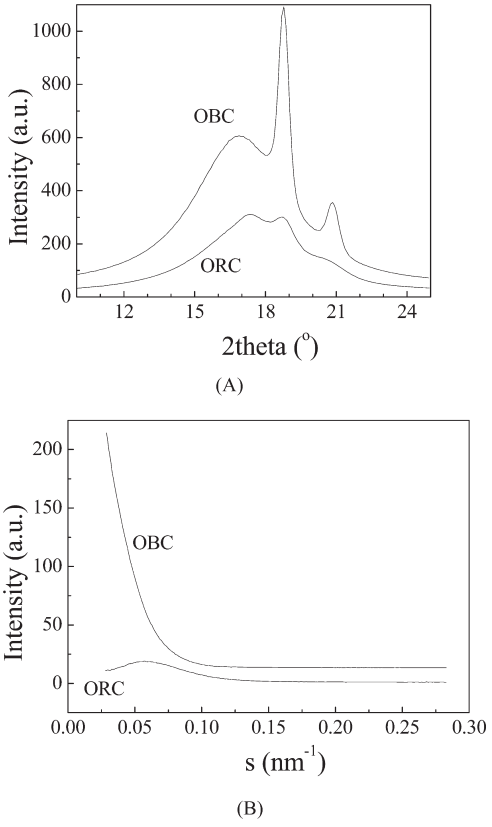

Figure 8. Integrated WAXD (A) and SAXS (B) profiles of OBC and ORC at room temperature before deformation.

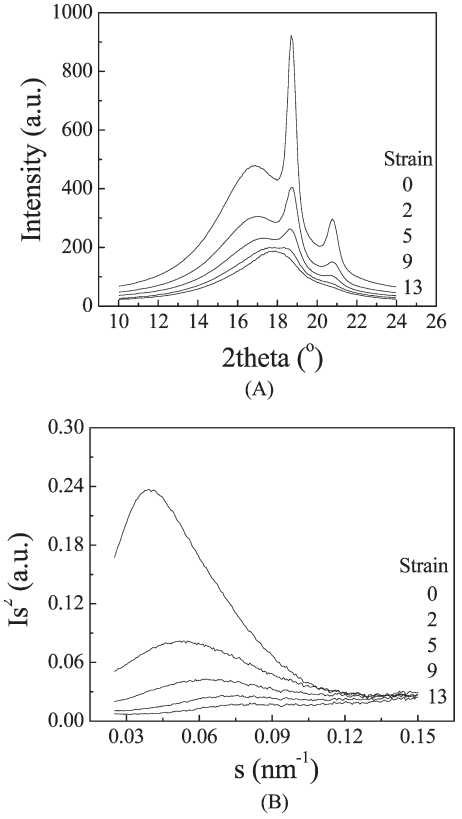

Figure 9. (A) Selected integrated WAXD profiles of OBC during deformation. (B) Selected Lorentz-corrected integrated SAXS profiles along meridian of OBC during deformation.

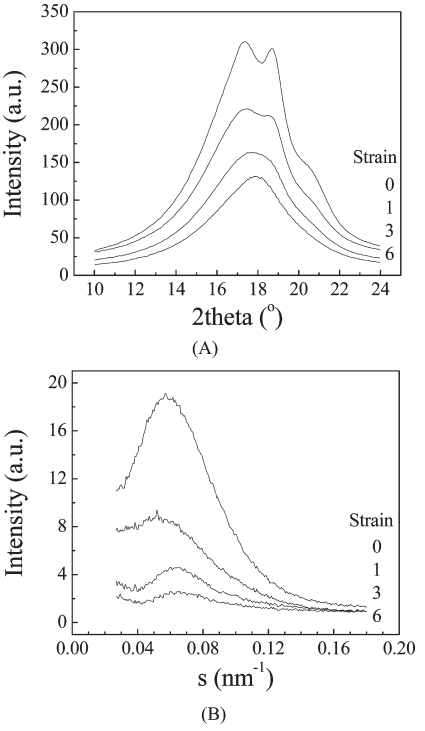

Figure 10. (A) Selected integrated WAXD profiles of ORC during deformation. (B) Selected integrated SAXS profiles along meridian of ORC during deformation.

peak in ORC is at a higher angle than OBC; in fact, it is closer to that of the hexagonal (100) reflection. This suggests that some crystals in the form of the hexagonal phase might exist in ORC. The integrated SAXS profile from the initial ORC sample shows a typical lamellar scattering pattern (Figure 8B), which is quite different from the diffuse scattering feature from OBC. No sign of a SAXS equatorial streak was observed throughout the process of deformation in ORC.

Selected integrated WAXD profiles of OBC during deformation at different strains are shown in Figure 9A. With the increasing strain, the heights of both (110) and (200) reflections relative to that of the amorphous peak decreased. In addition, the amorphous peak becomes broader and shifts to a higher angle due to both the decreasing *d*-spacing of amorphous chains and the emergence of the (010) reflection from the monoclinic phase induced by deformation, and the latter one should be a major contribution. When the strain is larger than 9, it is difficult to separate (110) and (200) reflections from the broad overlap of the amorphous peak and the monoclinic (010) reflection, which means that the fraction of the orthorhombic phase cannot be estimated using the 1D peak fitting method. This is quite evident for the WAXD profile at strain = 13, where only one broad peak is observed, which includes contributions from orthorhombic and monoclinic phases as well as the amorphous phase. Lorentz-corrected SAXS intensity profiles along the meridian in OBC at different strains are shown in Figure 9B. The *s* value at the scattering maximum after Lorentz correction is used to determine the long period between the adjacent lamellar layers. The shifting of the peaks to the high *s* value with the increase of strain indicates that the long period is decreasing during deformation along the meridional direction. This implies that fragmentation of the lamellar structure took place, resulting in some smaller but larger population of lamellar crystals in OBC under high strains.

Selected integrated WAXD and SAXS profiles of ORC during deformation at room temperature are shown in Figure 10. Similar to OBC, new monoclinic crystals induced by deformation are also found, in addition to the original orthorhombic and hexagonal crystals in the initial sample. The (010) reflection from the monoclinic phase becomes much more intense at high strains (also can be seen from the strong point-like scattering from the monoclinic phase in Figure 7), resulting in a single broad peak with its maximum between those of amorphous and orthorhombic (110) peaks. However, the corresponding peak position of the meridional scattering maximum in SAXS does not change dramatically as that in OBC. The calculated long periods of OBC and ORC along the meridional direction are illustrated in Figure 11. It is found that the long period decreases continuously with strain in OBC, while it increases at the early stage of deformation, then decreases only slightly, and later reaches a plateau value in ORC. This indicates that fragmentation of lamellar crystals in ORC is probably significantly less than that in OBC under high strains.

Deformation at High Temperature (60 °C). *In situ* SAXS and WAXD experiments during uniaxial deformation on both samples were also carried out at 60 °C. The evolution of 2D WAXD and SAXS patterns at this temperature was similar to that at room temperature, but at a slow rate due to the high mobility of polymer chains. 2D WAXD and SAXS patterns collected right before fracture are shown in Figure 12. It is seen that, upon the fracture point, OBC reaches significantly lower orientation compared to the corresponding state at room temperature. In addition, only the monoclinic form of low fraction is obtained at 60 °C, whereby the (010) reflection is very weak. The final orientation in ORC under deformation at 60 °C is significantly

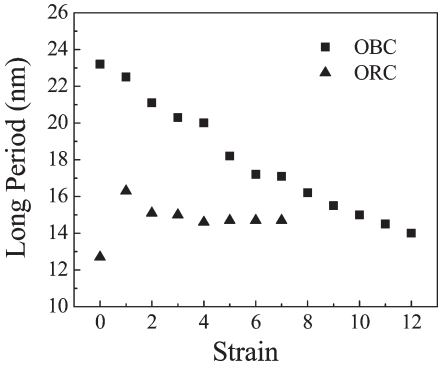

Figure 11. Change of meridional long period during deformation at room temperature.

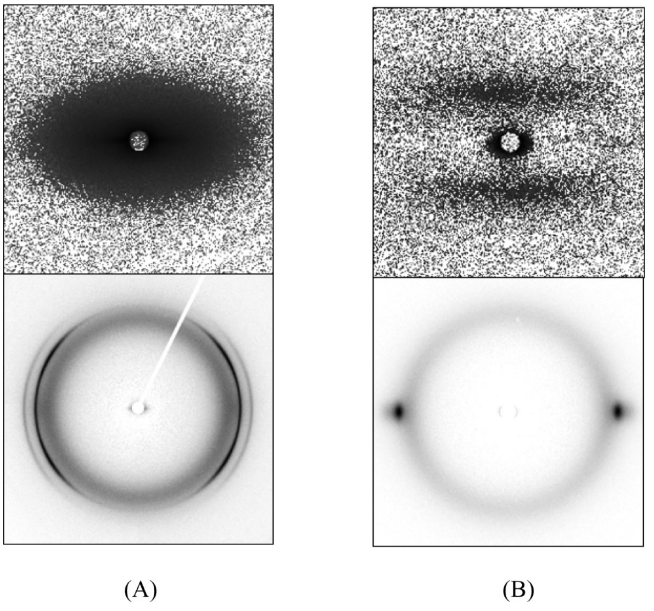

Figure 12. 2D SAXS and WAXD patterns of OBC (A) and ORC (B) right before fracture during deformation at 60 °C (strain = 4.4 and 8.3 for OBC and ORC, respectively).

better, and one apparent reason is that the fracture strain is relatively high. Its corresponding 2D WAXD pattern (Figure 12) indicates that intense point-like reflections are formed on the equator, separated from the amorphous halo. This indicates that only the orthorhombic form is induced by tensile deformation of ORC at 60 °C, instead of the monoclinic form. Comparisons between integrated WAXD profiles of ORC obtained at room temperature and at 60 °C are shown in Figure 13. Before deformation (i.e., strain = 0), the peak positions of the first reflections are not the same at different temperatures. As discussed earlier, because of the existence of the hexagonal form at room temperature, the amorphous peak shifted to the high angle, which superimposed with the hexagonal (100) reflection. However, this peak shifted back to the position exactly the same as that of OBC when the sample was heated to 60 °C. This suggested that the hexagonal crystals are melted at this temperature. Furthermore, it is found that at strain = 8 at room temperature this peak is shifted to the position of the monoclinic (010) reflection, while at 60 °C, this peak remains unchanged. This indicates that the monoclinic form could hardly be induced by deformation at 60 °C, which is because the monoclinic form is not stable at high temperatures due to the low stress on the sample.

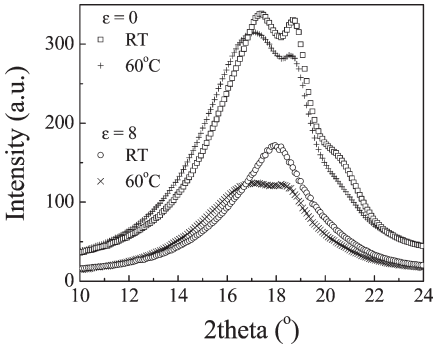

Figure 13. Comparison of integrated WAXD profiles of ORC at different temperatures and strains.

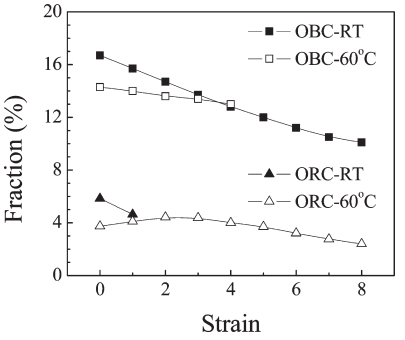

Figure 14. Evolution of the fraction of orthorhombic crystals in OBC and ORC during deformation.

Structure Analysis during Deformation. The fractions of the orthorhombic form in OBC and ORC during uniaxial tensile deformation were calculated using the 1D peak fitting method. We assumed that the stretched sample had a cylindrical symmetry around the deformation axis, where the 2D WAXD pattern could be used to determine the fraction of each phase. Since the amorphous reflection is superimposed with the monoclinic (010) reflection and cannot be deconvoluted by 1D peak fitting, we only estimated the total area of orthorhombic (110) and (200) reflections, which are intense and can be easily separated from the broad reflection at the early stage of deformation. As a result, the fraction of the orthorhombic phase, estimated from the area ratio of orthorhombic (110) and (200) reflections and total diffraction, is determined. The results are illustrated in Figure 14. At room temperature, the fraction of the orthorhombic phase in OBC decreases from about 17% to 10% as strain increases from 0 to 8 (above strain = 8, as orthorhombic reflections could not be separated from other diffraction peaks, no estimate was made). The fraction of the orthorhombic phase is lower in ORC due to the disrupting role of the octene comonomer during crystallization. It is interesting to observe that the formation of monoclinic phase in ORC is faster upon deformation by comparing the appearance of strong point-like scattering from monoclinic phase in Figures 3 and 7, resulting in a single broad peak containing all reflections. As a result, the fraction of the orthorhombic phase cannot be calculated when strain is greater than 1. At 60 °C, a slower decreasing of the orthorhombic phase in OBC than that at room temperature is observed. In ORC, the recrystallization process is quite notable at 60 °C, where a slight increase in the fraction of the orthorhombic phase is first observed at low strains, followed by the decrease of the orthorhombic fraction. This is consistent with the hypothesis that the monoclinic phase is

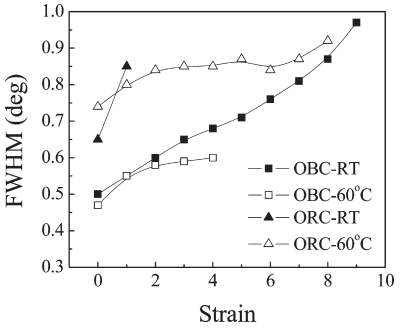

Figure 15. Change of FWHM of the orthorhombic (110) reflection during deformation.

not stable at high temperatures compared with the orthorhombic phase.

The full width at half-maximum (FWHM) of the orthorhombic (110) reflection as a function of strain is shown in Figure 15. According to the Scherrer equation, the crystal size is inversely proportional to the FWHM, but during uniaxial deformation, the microstrain and distortion of the second kind may also affect the FWHM. However, given that the experimental conditions were the same for both samples, the comparison of FWHM should still reveal the changes of crystal size between samples during deformation. On the basis of results in Figure 15, smaller crystals are found in ORC, and it could be attributed to the poor crystallizability due to the disruption of the octene comonomer. It is found that the FWHM increases upon deformation, indicating that the corresponding crystal size decreases with strain. This might be because lamellar crystals are fragmented due to the chain pulling-out mechanism. The decreasing rate of the crystal size is higher at room temperature than that at 60 °C, indicating that fragmentation took place easily at room temperature, consistent with our previous results in deformation of iPP,[30] which was explained from the relative strength of the entangled amorphous network at different temperatures.

The degrees of orientation of the amorphous and crystal phases were calculated based on Hermans' orientation function:[31]

$$f = \frac{3\langle\cos^2\phi\rangle - 1}{2}$$

where ϕ is the angle between the chain axis and the reference axis (stretching direction). $\langle\cos^2\phi\rangle$ is defined as

$$\langle\cos^2\phi\rangle = \frac{\int_0^{\pi/2} I(\phi)\cos^2\phi\sin\phi\,\mathrm{d}\phi}{\int_0^{\pi/2} I(\phi)\sin\phi\,\mathrm{d}\phi}$$

where $I(\phi)$ is the scattered intensity along the angle ϕ. The range of Hermans' orientation function is in the range of -0.5 to 1. Since there is no plane of symmetry perpendicular to the chain axis, i.e., the *c*-axis orientation could not be measured directly due to the absence of (00*l*) plane, we obtained the crystal orientation indirectly from the (110) and (200) reflections using the following expression

$$\langle\cos^2\phi\rangle = 1 - 1.435\langle\cos^2\phi_{110}\rangle - 0.565\langle\cos^2\phi_{200}\rangle$$

Regarding the amorphous phase, the orientation we calculated was actually that of the normal vector of the amorphous chains. Thus, the *f* value was multiplied by a factor of -2 to convert the orientation factor (-0.5 to 0) into the value (1 to 0) representing the degree of orientation along the stretching direction. When $f = 1$, it means all polymer chains are aligned with the stretching direction perfectly; when $f = -0.5$, it means that the chains are all aligned perpendicularly to the stretching direction; and $f = 0$, indicating random orientation of the chains. In estimating the orientation of the amorphous phase, the azimuthal scan was chosen along a lower *s* value at 2.04 nm^{-1} instead of the amorphous peak position at 2.13 nm^{-1} in order to reduce the contribution from the (010) reflection.

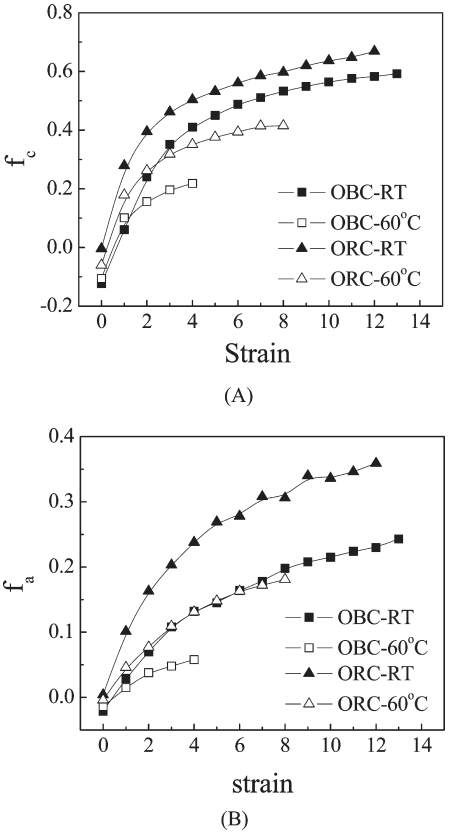

Figure 16. Hermans' orientation factors of (A) crystal and (B) amorphous phases as a function of strain.

The estimated Hermans' orientation factors of crystal and amorphous phases as a function of strain are shown in parts A and B of Figure 16, respectively. The orientation of both phases increase asymptotically toward the value of unity upon deformation, representing the improved alignment of polymer chains along the stretching direction. The orientation of the crystal phase is higher than the amorphous phase, which can be explained by the easy relaxation of the amorphous chains. It is found that the degrees of orientation of both phases in ORC are always higher than those in OBC, which is consistent with our explanation before about the connectivity among the chains and effectiveness of the network in ORC and OBC. Clearly, better connectivity and more effective network in ORC lead to higher orientation of the polymer chains upon uniaxial deformation.

Conclusions

ORC and OBC (ethylene−octene random and block copolymers, respectively) with similar overall density were uniaxially stretched at room temperature and 60 °C. Engineering stress−strain curves and 2D SAXS and WAXD patterns were collected simultaneously using *in situ* synchrotron X-rays. OBC showed a better crystallizability than ORC due to the low octene content and high density of long hard blocks. The crystals formed in OBC

were mainly in the orthorhombic form, but for ORC the hexagonal form was also coexistent with the orthorhombic form. Upon deformation at room temperature, the fraction of the orthorhombic form decreased in both samples, and the monoclinic form was induced. While at 60 °C, only the orthorhombic form was dominant, indicating that the monoclinic form was unstable at high temperatures. The fracture strain of OBC is much smaller than ORC at 60 °C. This can be attributed to the effectiveness of the network, which is due to the molecular weight distribution and chain architecture, and α-relaxation of the polyethylene crystals. The Hermans' orientation factors of both amorphous and crystal phases were estimated, and better orientation in ORC than that in OBC under deformation was observed, which is also because of the better connectivity and more effective network in ORC.

Acknowledgment. The authors thank the National Science Foundation (DMR-0906512) for the financial support. The assistance of Drs. Lixia Rong and Jie Zhu for synchrotron SAXS and WAXD experimental setup is also greatly appreciated.

References and Notes

(1) Arriola, D. J.; Carnahan, E. M.; Hustad, P. D.; Kuhlman, R. L.; Wenzel, T. T. *Science* **2006**, *312*, 714–719.
(2) Arriola, D. J.; Carnahan, E. M.; Cheung, Y. W.; Devore, D. D.; Graf, D. D.; Hustad, P. D.; Kuhlman, R. L.; Shan, C. L. P.; Poon, B. C.; Roof, G. R.; Stevens, J. C.; Stirn, P. J.; Wenzel, T. T. Catalyst composition comprising shuttling agent for ethylene multi-block copolymer formation. WO 2005090427, 2005-US8917.
(3) Wang, H. P.; Khariwala, D. U.; Cheung, W.; Chum, S. P.; Hiltner, A.; Baer, E. *Macromolecules* **2007**, *40*, 2852–2862.
(4) Kamdar, A. R.; Wang, H. P.; Khariwala, D. U.; Taha, A.; Hiltner, A.; Baer, E. *J. Polym. Sci., Polym. Phys.* **2009**, *47*, 1554–1572.
(5) Khariwala, D. U.; Taha, A.; Chum, S. P.; Hiltner, A.; Baer, E. *Polymer* **2008**, *49*, 1365–1375.
(6) INFUSE Olefin Block Copolymers, The Dow Chemical Company, www.dow.com/infuse.
(7) Androsch, R.; Blackwell, J.; Chvalun, S. N.; Wunderlich, B. *Macromolecules* **1999**, *32*, 3735–3740.
(8) Androsch, R.; Stribeck, N.; Lupke, T.; Funari, S. S. *J. Polym. Sci., Part B: Polym. Phys.* **2002**, *40*, 1919–1930.
(9) Androsch, R.; Wunderlich, B.; Lupke, T.; Wutzler, A. *J. Polym. Sci., Part B: Polym. Phys.* **2002**, *40*, 1223–1235.
(10) Shan, H.; White, J. *Plast., Rubber Compos.* **2006**, *35*, 155–164.
(11) Hu, W.; Srinivas, S.; Sirota, E. B. *Macromolecules* **2002**, *35*, 5013–5024.
(12) Hu, W.; Sirota, E. B. *Macromolecules* **2003**, *36*, 5144–5149.
(13) Bensason, S.; Stepanov, E. V.; Chum, S.; Hiltner, A.; Baer, E. *Macromolecules* **1997**, *30*, 2436–2444.
(14) Eynde, S. V.; Rastogi, S.; Mathot, V. B. F.; Reynaers, H. *Macromolecules* **2000**, *33*, 9696–9704.
(15) Chen, H. Y.; Chum, S. P.; Hiltner, A.; Baer, E. *J. Polym. Sci., Part B: Polym. Phys.* **2001**, *39*, 1578–1593.
(16) Popli, R.; Glotin, M.; Mandelkern, L. *J. Polym. Sci., Polym. Phys. Ed.* **1984**, *22*, 407–448.
(17) Boyd, R. H. *Polymer* **1985**, *26*, 1123–1133.
(18) Nitta, K. H.; Tanaka, A. *Polymer* **2001**, *42*, 1219–1226.
(19) Chen, X.; Yoon, K.; Burger, C.; Sics, I.; Fang, D.; Hsiao, B. S.; Chu, B. *Macromolecules* **2005**, *38*, 3883–3893.
(20) Kiho, H.; Peterlin, A.; Geil, P. H. *J. Appl. Phys.* **1964**, *35*, 1599–1605.
(21) Kiho, H.; Peterlin, A.; Geil, P. H. *Polym. Lett.* **1965**, *3*, 157–160.
(22) Seto, T.; Hara, T.; Tanaka, K. *Jpn. J. Appl. Phys.* **1968**, *7*, 31–42.
(23) Takahashi, Y.; Ishida, T. *J. Polym. Sci., Part B: Polym. Phys.* **1988**, *26*, 2267–2277.
(24) Whttmann, J. C.; Lotz, B. *Polymer* **1989**, *30*, 27–34.
(25) Russell, K. E.; Hunter, B. K.; Heyding, R. D. *Polymer* **1997**, *38*, 1409–1414.
(26) Shan, H.; White, J. L. *Int. Polym. Process. XXI* **2006**, *4*, 361–373.
(27) Bates, F. S.; Hartney, M. A. *Macromolecules* **1985**, *18*, 2478–2486.
(28) Roe, R. J.; Fishkis, M.; Chang, J. C. *Macromolecules* **1981**, *14*, 1091–1103.
(29) Wang, H. P.; Chum, S. P.; Hiltner, A.; Baer, E. *J. Polym. Sci., Part B: Polym. Phys.* **2009**, *47*, 1313–1330.
(30) Zuo, F.; Keum, J. K.; Chen, X. M.; Hsiao, B. S.; Chen, H. Y.; Lai, S. Y.; Wevers, R.; Li, J. *Polymer* **2007**, *48*, 6867–6880.
(31) Wilchinsky, W. Z. *J. Appl. Phys.* **1960**, *31*, 1969.